Cavitation during high temperature deformation in Al-Mg alloys

Toda, Hiroyuki
Department of Mechanical Engineering, Toyohashi University of Technology

Shamsudin, Zul Azri Bin
Department of Mechanical Engineering, Toyohashi University of Technology

Shimizu, Kazuyuki
Department of Mechanical Engineering, Toyohashi University of Technology

Uesugi, kentaro
Japan Synchrotron Radiation Research Institute

他

出版情報：Acta materialia. 61 (7), pp.2403-2413, 2013-04-01. Elsevier
バージョン：
権利関係：

Cavitation during high temperature deformation in Al-Mg alloys

Hiroyuki Toda[a], Zul Azri Bin Shamsudin[a], Kazuyuki Shimizu[a], Kentaro Uesugi[b], Akihisa Takeuchi[b], Yoshio Suzuki[b], Mitsuru Nakazawa[c], Yoshimitsu Aoki[d], Masakazu Kobayashi[a]

[a] Department of Mechanical Engineering, Toyohashi University of Technology, Toyohashi, AICHI 441-8580, Japan.

[b] Japan Synchrotron Radiation Research Institute, Sayo-gun, HYOGO 679-5198, Japan.

[c] Department of Intelligent Media, Osaka University, Ibaraki, OSAKA 567-0047, Japan.

[d] Department of Electronics & Electrical Engineering, Keio University, Yokohama, KANAGAWA 223-8522, Japan.

Abstract

It has recently been revealed that high-density pre-existing hydrogen micro pores, formed during production processes, exhibit premature growth and coalescence under external loading at room temperature, thereby inducing ductile fracture. This process is incidentally supplemented by the well-established ductile fracture mechanism based on particle damage. It is reasonable to assume that the pre-existing hydrogen micro pores may also contribute to damage evolution at high temperatures. In the present study, synchrotron X-ray microtomography was applied to the in-situ observation of

deformation and fracture in Al-Mg alloys at a high temperature. High-density hydrogen micro pores were observed in the alloys. Flow localization controlled deformation through the mechanism of solute drag creep. A combined effect of grain boundary sliding and heterogeneous nucleation on particles was also confirmed to accelerate the growth of pre-existing hydrogen micro pores and cavities. Although continuous nucleation occurred together with the growth of pre-existing hydrogen micro pores, the effects of the pre-existing hydrogen micro pores, especially those located on grain boundaries, were predominant in the overall damage evolution. It seemed likely that supersaturated hydrogen in the aluminum alloys might also make an appreciable contribution to cavitation during high temperature loading.

1. Background

During the last decade, attempts have been made to introduce the quick plastic forming process (QPF) into the automotive industry [1]. QPF takes place at even higher forming rates and lower temperatures than superplastic forming (SPF), resulting in successful implementation of QPF as a cost-effective and higher-volume manufacturing alternative to SPF in the case of aluminum alloy components. The major mechanism of deformation in the case of SPF is grain boundary sliding (GBS) [2,3], while a combined contribution of GBS and solute drag creep (SDC) is indispensable in the case of QPF [2,3], preserving a relatively large strain rate sensitivity parameter, m, and hence reasonable deformability.

Hot formability is, however, often limited by cavitation during forming, making cavity formation, growth and coalescence behavior an issue of primary importance in improving deformability [2-6]. It has been reported that cavities unidirectionally align along the tensile axis, exhibiting a stringlike formation [2, 7], under conditions in which SDC controls deformation; while cavities coalesce perpendicularly to the tensile axis, with more isotropic spatial distribution, during GBS [2, 7]. Possible cavitation mechanisms include (1) GBS leading to stress concentration at triple junction points and/or grain boundary ledges, (2) cracking of particles, especially those located on grain boundaries, and (3) vacancy condensation on grain boundaries [8, 9]. Kassner et al. reported that cavity nucleation only occurred on high-angle grain boundaries with grain boundary particles [10]. It has also been frequently reported that transverse grain boundaries are common locations for cavitation [9]. It is, however, still not well established by what mechanism and at which locations cavities nucleate.

Meanwhile, high-resolution X-ray microtomography has revealed the existence of high-density micro pores in most aluminum alloys, due to the precipitation of molecular hydrogen [11, 12]. The hydrogen content in aluminum alloys is usually three to four orders of magnitude larger than the hydrogen solubility in solid aluminum alloys, due mainly to the existence of a hydrogen solubility gap at the melting temperature of aluminum, and the presence of a surface oxide layer. It has been reported that supersaturated hydrogen in solid aluminum is predominantly partitioned to micro pores [11]. The trap site occupancies of normal interstitial lattice sites, solute atoms, dislocations and grain boundaries are elevated with increases in hydrogen content [11]. The number density of micro pores exceeds 10,000 per 1 mm^3 in most wrought aluminum alloys [13], and it has been reported that the hydrogen micro pores do not close even through subsequent extensive hot and cold plastic deformation [12, 14]. Moreover, it has recently been discovered, by the present authors, that such micro pores exhibit premature growth under external loading at room temperature, thereby inducing ductile fracture [14, 15]. The well-known particle fracture mechanism operates only incidentally during the ductile fracture of aluminum alloys [14, 15].

Given the recently revealed effects of micro pores on room temperature deformation, it is reasonable to assume that pre-existing hydrogen micro pores may also contribute to damage evolution at high temperatures, at least to some extent. In the present study, synchrotron X-ray microtomography was applied to the in-situ observation of deformation and fracture in Al-Mg alloys at a high temperature. Such high-resolution 3D/4D (i.e., 3D plus time axis) imaging readily enables the visualization of individual cavities throughout deformation, providing a unique opportunity to quantitatively analyze the initiation, growth and coalescence of each cavity. In addition

to this visualization of cavities and particles, crystallographic grains were visualized by doping gallium into grain boundaries, thereby identifying the location where each cavity nucleated.

2. Experimental methods

2.1 Sample preparation

High-purity and low-purity 5086 alloys (hereinafter HP and LP, respectively) were obtained from Furukawa-Sky Aluminum Corp. Alloy LP had a chemical composition of 4.5 Mg, 0.7 Mn, 0.12 Cr, 0.20 Fe, 0.15 Si and the balance as Al in mass percent. Alloy HP had a chemical composition of 4.5 Mg, 0.7 Mn, 0.13 Cr, 0.04 Fe, 0.04 Si and the balance as Al in mass percent, being characterized as a low Cr and Si alloy suitable for SPF. Another Al-Mg alloy, with reduced Mn and Cr content (hereinafter HP-C, as a coarse-grained high-purity alloy), was specifically prepared for identifying the location where each cavity nucleated. Alloy HP-C had a chemical composition of 4.5 Mg, 0.2 Mn, 0.0 Cr, 0.03 Fe, 0.02 Si and the balance as Al in mass percent, and is not compatible with the industrial standard of 5086 alloy due to its low Cr content. Almost all of the grains in alloys HP and LP had grain size smaller than 10 μm, whereas those of HP-C typically ranged between 50 and 200 μm. Tensile specimens similar to those used in the previous study [14] (0.6 (Width) × 0.6 (Thickness) × 3 (Length) mm in gauge section) were machined from as-received 1.3 mm thick plates, using an electro-discharge machine wire eroder, with tensile load applied in the rolling direction.

2.2 Tomographic imaging

A high-resolution X-ray CT experiment was performed using the X-ray imaging beamline, BL20XU, of the SPring-8 facility. Samples were positioned in Experimental Hutch 1, which is located approximately 80 m from the X-ray source. A monochromatic X-ray beam, with a photon energy of 20 keV, generated by a liquid nitrogen-cooled Si (111) double crystal monochromator, was used. The image detector consisted of a cooled 4000 (H) × 2624 (V) element CCD camera (with effective pixel size of 5.9 μm, and used in 2 x 2 binning mode), a single crystal Lu_2SiO_5:Ce scintillator, and a ×20 lens. The image detector was positioned 60 mm behind the sample, thereby making the imaging system sensitive to phase modulation. In total, 1500 radiographs, scanning 180 degrees, were obtained in 0.12-degree increments. The entire cross-section of the specimen and a region about 551 μm high were captured on the CCD camera. Image slices were reconstructed from a series of projections based on the conventional filtered backprojection algorithm. An isotropic voxel with a 0.42 μm edge was achieved in the reconstructed slices. The grey value in each dataset was calibrated such that the linear absorption coefficient of 0 to 40 cm^{-1} fell within an 8-bit gray scale range between 0 and 255.

In-situ tensile tests were performed using a material test rig specially designed by the present authors for X-ray CT observation at high temperatures. An amorphous carbon tube was used as an axisymmetric load frame, resulting in negligible X-ray absorption. The test rig was equipped with upper and lower microring heaters (220V-340W each) to heat the tomographic specimens to 923 K. Thermal drift of a specimen could be suppressed to some extent by circulating water through channels machined in the upper and lower components. Tomographic scans were performed at 773 K, at successive increments of applied cross-head displacement, while holding a

sample at fixed cross-head displacements. Approximate strain rate during loading was 10^{-2}. The displacement vector in the loading direction measured between a couple of particles that are located near the upper and lower edges of the field of view, which specifies the relative position of the particle in reference to its previous position, was used to calculate the applied strain in the loading direction. The tensile test of alloy HP-C was interrupted well before the final rupture, in order to apply gallium for grain boundary visualization [16, 17]. Only one in-situ tensile test was performed for each material due to severe time constraints in the synchrotron experiment.

2.3 Image analysis

2.3.1 Quantitative evaluation of particles and cavities

To estimate the volume of each micro pore/cavity with sub-voxel accuracy, pentagonal facetted iso-intensity surfaces were computed from the volumetric data set using the conventional Marching Cubes algorithm [18]. The threshold value for obtaining binary images was set at 9 and 190 for micro pores/cavities and particles, respectively. To suppress inaccuracies originating from image noise, only micro pores over 23.168 voxels in volume were counted as microstructural features in the quantitative analysis. The image data were processed using home-made software.

2.3.2 3D strain mapping via particle tracking

Precise image registration was then performed before microstructural features were tracked, using a transformation matrix, which minimizes the sum of the distances between identical microstructural features captured at neighboring scan steps. The

matching parameter method with the modified spring model [19, 20] was employed for tracking particles throughout loading. The coefficients α, β and γ, and the search range in the matching probability parameter, all as in Kobayashi et al. [19, 20], were determined to be 0.8, 0.1, 0.1 and 10 μm, respectively, after systematically searching for the optimum condition in a preliminary trial in which a success ratio close to 100 % was achieved. All the visible particles were tracked in chronological order.

Tetrahedrons with vertices occupied by particles were generated by the Delaunay tessellation technique [21]. All the strain components were calculated from the deformation of the tetrahedron, assuming a linear displacement field, which is a set of displacement vectors for all the voxels, within it.

2.3.3 Reverse cavity tracking

All the visible cavities were tracked regressively, from the final loading step toward the initial stress-free state, in order either to identify the loading step at which each cavity was initiated or to identify the given cavity as a pre-existing hydrogen micro pore. During high temperature deformation, cavities may be classified into two types: one remains intact until the next step, and can be successfully tracked over the increment; the other has coalesced with a neighboring cavity, and so cannot be tracked. Considerable cavity coalescence occurs due to the high applied strain during high temperature tension, rendering standard microstructural tracking, such as that described in Section 2.3.2, ineffective in cavity tracking. A trajectory prediction procedure was therefore applied for tracking the cavities in the present study. When two or more cavities have coalesced at loading step *n*, the physical displacement of particles located within a search area of radius *R*, between steps *n*-1 and *n*, may be used to predict a

complex trajectory for the cavities. Scattered data interpolation using radial basis functions was here employed to predict the physical displacement of each cavity. The details of the trajectory prediction procedure are available elsewhere [12, 20]. In the present study, the value of *R* was determined to be 6.3 μm, based on the identification of at least five particles within the search area.

2.3.4 Identification of cavity nucleation sites

The locations of cavities are closely associated with the exact mechanism of cavity nucleation, which has been difficult to ascertain through conventional observation. Although GBS provides a rough measure of the displacement field occurring during high temperature deformation, it is important to investigate whether cavity nucleation requires the existence of second phase particles. In the present study, cavities located on grain boundaries were distinguished from those located in the grain interior [22]. For this, precise image registration was performed using the tomographic images captured before and after gallium application. The 3D gallium image was first segmented, after selecting an appropriate threshold for the linear absorption coefficient, and then used to classify cavities into grain boundary and grain interior varieties, according to their gravity center locations. Only grain boundary cavities were extracted, by extracting cavities that partially overlapped between the two 3D images, using an image processing algorithm.

In addition, it was determined whether cavities were attached directly to particles or whether matrix aluminum intervened. Cavities nucleated heterogeneously on particles were distinguished, regardless of whether they were located on grain boundaries or in the grain interior. The details of the organizational scheme are

described elsewhere [11].

3. Initial microstructural features

Figure 1 (a) shows the 3D distribution of the dispersion particles and cavities before loading, within the volume of interest (176 × 252 × 349 μm), in alloy HP. Underlying aluminum is not displayed in the figure. The number density of dispersion particles with X-ray absorption higher than that of aluminum is 0.88×10^{-10} and 1.98×10^{-10} m^{-3} in alloys HP and LP, respectively. Although average particle size does not greatly differ (2.5 and 2.9 μm for alloys HP and LP, respectively), the particle volume fraction is approximately four times larger in alloy LP (0.60 %) than in alloy HP.

Similar configurations of pre-existing hydrogen micro pores are observed in the two alloys before loading (number density / average pore size / volume fraction are 0.31×10^{-10} m^{-3} / 2.6 μm / 0.04 % and 1.45×10^{-10} m^{-3} / 2.7 μm / 0.23 % for alloys HP and LP, respectively). Almost all the large hydrogen micro pores appear to be nucleated heterogeneously on particles, as shown in Fig. 1 (a). It has been reported by the present authors that at least 60 % of micro pores had been formed heterogeneously on constituent particles in Al-5.5Mg alloys, and that vacancies are not involved in the formation process of micro pores [11]. In terms of subsequent particle cracking, almost all the coarse particles are covered by a few micro pores. Although particles' angular shape may result in forceful constraint of matrix flow around them during loading, which accordingly increases the internal stress in the particles, the existence of hydrogen micro pores on particles is attributable to the relaxation of the particle stress, thereby suppressing particle cracking effectively.

4. Material flow

Figure 2 shows the measured effective strain distributions across the tomographic specimen. Effective strain appears relatively uniform during the first loading, while strain localization is apparent between macroscopic applied strains of 0.5 and 0.74. As opposed to the uniform strain distribution shown in Fig. 2 (a), it has been reported by the present authors that macroscopic shear banding is observed under macroscopic monotonic compression at room temperature, as shown in Fig. 8 of the previous article [12]. When examined more closely, yellow or red regions are sparsely seen in Fig. 2 (a), which shows an effective strain several times higher than 0.28 (i.e., macroscopic applied strain: the blue to green contour level), indicating that some limited regions are locally exposed to intense strain. This local scattering might be the cause of the premature cavitation revealed later. More extensive strain localization is observed in Fig. 2 (b), where more red regions are concentrated near the top of the field of view. This is associated with flow localization. Kulas et al. quantified the degree of flow localization by defining the following Q parameter [2]:

$$Q = \frac{q - q^*}{q^*} \tag{1}$$

where q is reduction in area at the point of failure, q^* is reduction in area value without flow localization. q^* is determined by Eq. (2).

$$q^* = \left(1 - \frac{1}{1 + e_f}\right) \quad (2)$$

where ε_f is elongation to failure. Kulas et al. have reported that flow localization is dominant (i.e., positive Q values) above the Zener-Hollomon parameter, Z, of $3x10^5$ / s, for an AA5083 alloy similar to alloy LP of the present study [2]. Calculated Q values for alloys LP and HP are 23.0 and 17.7, respectively, for a Z value of 2.7×10^5 / s, under the assumption of activation energy of Q_c = 110 kJ / mole, indicating that flow localization controls fracture under deformation in the case of the SDC mechanism. Consistent with the previous report would be the fact that commercial 5000-series aluminum alloys deforming under SDC exhibit flow localization, whereas the final rupture is caused by cavity growth and coalescence [2].

5. Cavitation

5.1 Overall growth behavior

3D quantitative measurements of cavity volume fraction as a function of strain are shown in Fig. 3. As has often been reported regarding cavity growth, the relationship between cavity volume fraction, V_f, and strain, ε, can be well described by the expression:

$$V_f = V_0 exp(\eta\varepsilon) \quad (3)$$

where V_0 is the initial volume fraction of cavities and η is a cavity growth constant. The strong experimental correlation between changes in cavity volume fraction and Eq. (3) is an indication that cavity growth would appear to be plasticity controlled [2]. The

deviation from Eq. (3) and slight difference in η, seen in Fig. 3, are attributable to the contribution from newly initiated cavities during loading, which is not captured in the equation. This is because cavity initiation during loading is more frequent in alloy HP than alloy LP, as shown later in the paper. V_f is 1.34 and 2.93 % immediately before the final rupture in alloys HP and LP, respectively. It has been claimed that cavity volume fraction in excess of 2 % is sufficient to degrade mechanical properties beyond acceptable performance requirements [23]. Du et al. have conducted a numerical simulation by modeling SDC, GBS and grain boundary diffusion [24], and reported that cavity growth rate depends on cavity size. The reported η values are 8.77 and 5.46 at a strain rate of 3×10^{-4} and 3×10^{-2} s^{-1}, respectively, for AA5083. The simulation assumed a ratio of void volume, V, to grain volume, V_g, of 0.229. In the present study, the η values are 3.0 to 3.9, at a strain rate of 10^{-2} s^{-1}, for V/V_g of 0.25 to 0.27. The discrepancy may be a result of the different model dimensions (2D and 3D) and/or size effects of the tiny tomographic specimens.

Actual cavity nucleation and growth behavior are also shown in Fig. 1, where an identical region is displayed throughout loading. It is well-known that SDC becomes a dominant deformation mechanism under high strain rates at low temperatures [25]. In fact, it has been reported that an AA5083 alloy with a chemical composition and grain size similar to alloy LP of the present study exhibits SDC at 723 K at a strain rate of 3×10^{-2} / s, while GBS is observed at 723 K at a strain rate of 3×10^{-4} / s [2]. Cavities unidirectionally aligned along the tensile axis, which are typical of SDC-controlled deformation [2, 7], are seen in Fig. 1. Since the cavity growth rate, $dr / d\varepsilon$ (r: cavity radius, ε: macroscopic strain), is inversely proportional to r^2 [2], diffusion-controlled cavity growth is predominant only when cavities are well below 1 μm in diameter [5].

In the present study, the majority of cavities are larger than 2 μm in diameter, and the strain rate is relatively high. This implies that diffusion does not contribute to the cavitation behavior. According to Du et al.'s prediction [24], the fraction of void growth through SDC, GBS and grain boundary diffusion is roughly 0.65, 0.3 and 0.05, respectively. It is therefore reasonable to assume that GBS-controlled deformation occurring in a complementary manner may also cause some damage along grain boundaries.

5.2 Cavity shape

It has been shown that crack-like cavities are formed due to GBS, especially in the case of higher strain rates and closely located cavities [26]. This is inconsistent with the rather spherical cavities shown in Fig. 1, suggesting that general cavity growth does not substantially involve GBS. It is also worth noting that examination of the fracture surfaces revealed a dimpled pattern typical of transgranular ductile fracture, in both alloys LP and HP. Cavities, especially those nucleated on particles, exhibited a rather complex shape. This is probably due to the complex stress field in the vicinity of the particles, resulting from the presence of the particles. In this regard, the volume change of each cavity is plotted, in Fig. 4, as a function of the local strain, measured by tracking particles. It is obvious that the magnitude and sign of the local strain cannot be associated with cavity growth. In the present authors' room temperature rolling and shot-peening experiments, the annihilation behavior of micro pores was obviously dependent on the extent of the local plastic deformation of the aluminum matrix surrounding them, and the volume change of micro pores could be expressed as a function of the local effective strain [12, 27]. The strain distribution shown in Fig. 2 was

obtained by interpolating a local displacement field in each tetrahedron that was 10 to 100 μm across. This implies that cavity growth is dominated by more localized strain distribution in the vicinity of particles.

Another important consideration is the quantification of cavity shape change with loading. As is well-known, sphericity is a measure of how spherical an object is, and usually defined as the ratio of the surface area of a sphere to that of a given particle. Sphericity ranges between 0 and 1, and the closer the sphericity is to 1, the more spherical an object is. The average sphericity of hydrogen micro pores is 0.76, and this decreases to 0.61 immediately before the final rupture in alloy HP. The average sphericity of cavities newly initiated during the loading steps ranges between 0.85 (ε = 0.28) and 0.87 (ε = 0.82). The relatively high sphericity of such newly initiated cavities would appear to suggest the existence of molecular hydrogen inside these cavities. It is known that hydrogen is not readily lost, even with exposure during the homogenization, solution heat treatment and hot working of aluminum alloys, due to the presence of the thin but robust oxide film at the surface of these alloys, which acts to impede the release of hydrogen [28]. This implies that supersaturated hydrogen may make an appreciable contribution to cavitation in aluminum during high temperature loading.

5.3 Contributions of pre-existing pores and newly initiated cavities

The cavity growth data shown in Fig. 3 is organized according to the loading steps at which the cavities were initiated, and is summarized in Fig. 5 for alloy HP. It has been a matter of debate whether continuous nucleation of cavities occurs during loading [29, 30]. It is, however, obvious that continuous nucleation occurs together with the growth of pre-existing hydrogen micro pores (Fig. 5). It is interesting to note that the

cavity growth behavior of pre-existing hydrogen micro pores appears to be similar to that of newly initiated cavities, both in terms of cavity size and volume fraction. The value of the cavity growth parameter, *h*, is defined as follows [31]:

$$\frac{dr}{d\varepsilon} = \frac{h}{3}\left(r - \frac{3\gamma}{2\sigma_{eq}}\right) \tag{4}$$

where r is the radius and σ_{eq} is the von Mises equivalent stress. Eq. (4) does not address continuous cavity nucleation [6], and it is usually impossible to eliminate the effects of continuous cavity nucleation from macroscopic experimental measurement. The cavity growth rates of pre-existing hydrogen micro pores and newly initiated cavities are plotted as a function of average cavity radius in Fig. 6. It is noteworthy that only cavity growth behavior has been extracted and evaluated in Fig. 6. The cavity growth parameter slightly increases with the loading step at which cavities were nucleated. This is probably due to the slight increase in stress triaxiality generated with the flow localization. Since all the pre-existing hydrogen micro pores and cavities begin to grow from the moment of their nucleation, the earlier the hydrogen micro pores / cavities are nucleated, the larger the hydrogen micro pores / cavities become. In terms of the difference in number density between the pre-existing hydrogen micro pores and cavities nucleated at each loading step, the volume fraction of the pre-existing hydrogen micro pores at the final loading step is roughly one order of magnitude higher than that of the cavities that had been nucleated during the first loading, and roughly two to three orders of magnitude higher than that of the cavities nucleated during the subsequent loading steps, implying that the effects of the pre-existing hydrogen micro pores are predominant in the overall damage evolution behavior. It is reasonable to assume that

coarse pores / cavities are detrimental, leading to the final catastrophic fracture. Fig. 7 shows the histograms of cavities measured at the final loading step. The cavity size data shown in Fig. 3 is also organized according to the loading steps at which the cavities were initiated. Many coarse hydrogen micro pores, typically larger than 10 μm, are observed; whereas the majority of cavities are less than 10 μm, even including those nucleated during the first loading step.

The test temperature was 773 K in this study, which is suitable for QPF. Usually cavity growth rate increases with temperature. It may well be the case, however, that the overall damage evolution behavior at higher temperatures is nonetheless dominated by the presence of the pre-existing hydrogen micro pores.

5.4 Location of cavity nucleation

The locations where pre-existing hydrogen micro pores and cavities nucleate have been investigated for alloy HP-C. It should be noted that materials with fine grain size typically exhibit remarkable cavitation. The extent of cavitation may therefore differ between alloys HP-C and HP. A large difference in grain size sometimes dramatically alters cavitation mechanisms; and indeed, the fracture surface in alloy HP-C exhibited typical intergranular fracture.

The ratio of pores / cavities located on grain boundaries was 47.9, 71.5 and 71.7 % for cavities nucleated at a macroscopic applied strain of 0 (i.e., pre-existing hydrogen micro pores), 0.08 and 0.13, respectively. No particle cracking was observed in alloy HP-C, or in alloys HP and LP. The average diameter of cavities nucleated at a macroscopic applied strain of 0.08 did not differ greatly between grain boundary and grain interior cavities (3.0 and 1.9 μm, respectively), while the maximum diameter of

the cavities so nucleated was approximately three times larger in the case of grain boundary cavities than in that of grain interior cavities (11.0 and 3.8 μm, respectively). Roughly 37 % of all the cavities nucleated at a macroscopic applied strain of 0.08 were heterogeneously nucleated on particles; and the majority of such particles, playing the role of nucleation sites, were located on grain boundaries. Since an AlMg intermetallic compound has a linear absorption coefficient close to that of the aluminum matrix, there is a possibility that extremely small invisible particles provided nucleation sites for the cavities. However, such small particles may have limited potential to constrain matrix flow, resulting in the formation of relatively small and harmless cavities. It may therefore be concluded that cavity nucleation does not necessarily require the existence of second phase particles, whereas the existence of grain boundary plays an important role in cavitation. For example, Fig. 8, showing a magnified 3D-perspective view of alloy HP-C, reveals one pre-existing hydrogen micro pore, one homogeneously nucleated cavity located in the grain interior, and three heterogeneously nucleated cavities located on grain boundaries. It is clear that one of the three cavities located on the grain boundaries exhibited significant growth over two neighboring grain boundary planes; and it may be inferred that some additional condition, such as crystallographic orientation of the grain and its mismatch with a neighboring grain, may have some effect on such selective growth behavior. It has been well documented that cavities frequently nucleate on grain boundaries transverse to a tensile axis [9]. However, such a tendency was not confirmed in the present study.

Figure 9 summarizes the histograms of pre-existing hydrogen micro pores organized by location (grain boundary or grain interior), and nucleation mechanisms (homogeneous (independent) nucleation or heterogeneous nucleation on dispersion

particles). The number density of pre-existing hydrogen micro pores on grain boundaries was similar to that of the grain interior, and most such micro pores (roughly 90 %) were nucleated homogeneously in both cases. The pre-existing hydrogen micro pores located in the grain interior remained almost intact during the subsequent strain of 0.13, while those located along grain boundaries typically exhibited subsequent growth. The combined effect of localized deformation at grain boundaries and heterogeneous nucleation on particles produces accelerated growth, as shown in Fig. 9 (c). For example, Fig. 10 shows a magnified 3D-perspective view of alloy HP-C, with five pre-existing hydrogen micro pores seen in Fig. 10 (a). The four micro pores located in the grain interior remained almost spherical, with modest growth. On the other hand, the one micro pore located at a junction point of grain boundary planes was elongated and stretched into a L shape over the two neighboring grain boundary planes.

5.5 Discussion of the hydrogen micro pore mechanism

In our previous study [11], synchrotron X-ray microtomography was similarly used to observe the initiation and growth behavior of hydrogen micro pores, at high-temperature, in high-purity Al–Mg alloys with three different hydrogen contents, and in 99.999% pure aluminum. High-density hydrogen micro pores were observed in the high-purity Al–Mg alloys, while both the density and volume fraction were much lower in the case of the pure aluminum than in that of the high-purity Al–Mg alloys. This difference was attributable to the lack of hydrogen precipitation sites (i.e., dispersion particles) in pure aluminum [11]. The volume fraction of micro pores increased rapidly during simple thermal exposure at 823 K for 270 h, in all the Al-Mg alloys. In the present study, the test was 50 K lower than in our previous experiment,

suggesting that micro pore shrinkage and annihilation due to the thermal desorption of hydrogen do not occur for at least the few hundred hours monitored in the present study. The surface oxide film can be broken during loading at high temperatures, or during temperature variation, enabling the release of hydrogen. The latter cause of breakage is caused by the large discrepancy in thermal expansion between aluminum and its oxide [28]. It is therefore reasonable to assume that the desorption of hydrogen occurs only during loading at high temperatures and not during isothermal exposure without loading. This implies that even during typical SPF of 10^{-3} to 10^{-4} / s in strain rate and 1000 % at most in total elongation, which corresponds to an actual loading time of 2.8 ~ 28 h, micro pore annihilation never occurs, but instead its growth occurs without loading. It may be inferred that the hydrogen micro pore mechanism involved in high temperature cavitation may be predominant under a broad range of conditions in the case of aluminum alloys, but not in the case of pure aluminum. In fact, high density micro pores have been commonly observed in almost all industrial aluminum alloys, such as 1XXX, 2XXX, 5XXX, 6XXX and 7XXX-series alloys [13-15]. In a study by Toda et al. [11], total hydrogen content varied widely, between 0.3 and 5.12 ml / 100 g Al. The total amount of hydrogen trapped in micro pores was, however, similar in all three of the Al–Mg alloys in that study, while the trap site occupancy for dislocations and grain boundaries increased with an increase in the total amount of hydrogen. This implies that the hydrogen micro pore mechanism involved in high temperature cavitation may be predominant throughout the practical range of hydrogen content in aluminum alloys. It has been claimed that micro pores in aluminum alloys do not completely close even through extensive deformation by hot and cold rolling [12, 28]. Meanwhile, complete annihilation of micro pores was reported when utilizing the shot-peening treatment, in

which severe plastic deformation is achieved in a multi-axial state of stress. In this latter experiment, the shrinkage/annihilation behavior of micro pores could be interpreted as a function of the local effective strain [27]; and this may suggest the intriguing possibility that high temperature cavitation may be controlled by eliminating or reducing hydrogen micro pores through the application of such additional treatments.

It has been assumed that hydrogen in micro pores is in thermal equilibrium, where the surface tension, γ, is balanced by an opposing gas pressure inside each micro pore [11]. Internal pressure is calculated to be 0.46 and 4.6 MPa for r = 5 and 0.5 μm, respectively, under the assumption of γ = 1.16 N / m. The latter value is relatively close to the stress level during deformation from 773 (strain rate of 10^{-4}) to 823 K (strain rate of 5×10^{-3} to 5×10^{-4}). It is reasonable to assume that the hydrogen gas pressure inside micro pores makes an appreciable contribution to cavity growth, especially when the micro pores are less than 1 μm during SPF.

6. Summary

Synchrotron X-ray microtomography was employed to observe cavity nucleation and growth behavior in Al-Mg alloys. This approach enabled the reconstruction of distinct 3D renderings of pre-existing hydrogen micro pores, cavities and microstructural features with reasonable spatial resolution (i.e., about 1 μm). 3D strain mapping, reverse cavity tracking and nucleation site analysis, both for preexisting hydrogen micro pores and newly initiated cavities, were employed to analyze high-temperature cavitation behavior in the Al-Mg alloys. One important question was whether pre-existing hydrogen micro pores, which have recently been confirmed to

induce ductile fracture, could contribute to damage evolution at high temperatures. The experimental Al-Mg alloys exhibited flow localization with a dominant mechanism of solute drag creep, while the final rupture was caused by cavity growth and coalescence. The combined effect of the existence of grain boundaries and heterogeneous nucleation on particles was also confirmed to produce accelerated growth of pre-existing hydrogen micro pores and cavities. For example, the maximum cavity diameter was several times larger in the case of grain boundary cavities than in that of grain interior cavities. Although continuous nucleation occurred together with the growth of pre-existing hydrogen micro pores, the effects of the pre-existing hydrogen micro pores, especially those located on grain boundaries, were predominant in the overall damage evolution behavior. For example, the volume fraction and size of pre-existing hydrogen micro pores were dramatically different from those of cavities newly nucleated during loading. Indeed, many coarse hydrogen micro pores, which are typically larger than 10 μm, were observed after loading. It seemed likely that supersaturated hydrogen in the aluminum alloys may make an appreciable contribution to cavitation during high temperature loading.

Acknowledgements

This work was undertaken partly with the support of a Grant-in-aid for Scientific Research from JSPS through subject No. 20246102. The synchrotron radiation experiments were performed with the approval of JASRI through proposal Nos. 2009A1213 and 2010A1172. The support provided to HT by the Light Metal Educational Foundation is also gratefully acknowledged. The authors also thank Dr.

Katsumi Koyama and Dr. Koji Ichitani in Furukawa-Sky Aluminum Corp. for their assistance.

References

[1] Friedman PA, Copple WB. J Mater Eng Perf 2004;13:335- 347.

[2] Kulas MA, Green WP, Taleff EM, Krajewski PE, McNelly TR. Metall Mater Trans A 2006;37A:645–655.

[3] Krajewski PE, Schroth JG. Mater Sci Forum 2007;551-552:3-12.

[4] Verma R, Friedman P, Ghosh A, Kim S, Kim C. Metall Mater Trans A 1996;27A: 1889–1898.

[5] Pilling J. Mater Sci Technol 1985;1:461-466.

[6] Lombard CM, Ghosh AK, Semiatin SL. Metall Mater Trans A 2001;32A:2769-2779.

[7] Kawasaki M, Xu C, Langdon TG. Acta Mater 2005;53:5353-5364.

[8] Khaleel MA, Zbib HM, Nyberg EA. Int J Plast 2001;17:277-296.

[9] Kassner ME, Hayes TA. Int J Plast 2003;17:1715-1748.

[10] Kassner ME, Pérez-Prado MT. Prog Mater Sci 2000;45:1–102.

[11] Toda H, Hidaka T, Kobayashi M, Uesugi K, Takeuchi A, Horikawa K. Acta Mater 2009;57:2277-2290.

[12] Toda H, Minami K, Koyama K, Ichitani K, Kobayashi M, Uesugi K, Suzuki Y. Acta Mater 2009;57:4391-4403.

[13] Masuda S, Toda H, Aoyama S, Orii S, Ueda S, Kobayashi M. J JFS 2009;81:312-319. (in Japanese)

[14] Toda H, Oogo H, Uesugi K, Kobayashi M. Mater Trans 2009;50:2285–2290.

[15] Toda H, Oogo H, Inamori T, Tsuruta H, Horikawa K, Uesugi K, Takeuchi A, Suzuki Y, Nakazawa M, Aoki Y, Kobayashi M. Phil Mag A 2012, under review.

[16] Ludwig W, Nielsen SF, Poulsen HF, Bellet D. Defect and Diffusion Forum

2001; 1319:194–199.

[17] Kobayashi M, Toda H, Uesugi K, Ohgaki T, Kobayashi T, Takayama Y, Ahn BG. Phil Mag 2006;86:4351-4366.

[18] Lorensen WE, Cline HE. ACM Comput Graph 1987;21:163-169.

[19] Kobayashi M, Toda H, Kawai Y, Ohgaki T, Uesugi K, Wilkinson DS, Kobayashi T, Aoki Y, Nakazawa M. Acta Mater 2008;56:2167-2181.

[20] Toda H, Maire E, Aoki Y, Kobayashi M. J Strain Anal Eng Des 2011;46:549-561.

[21] Barber CB, Dobkin DP, Huhdanpaa HT. ACM Trans Math Softw 1996; 22:469-483.

[22] Toda H, Ohkawa Y, Kamiko T, Naganuma T, Uesugi K, Takeuchi A, Suzuki Y, Kobayashi M, Leclere DJ. Acta Mater 2012, under review.

[23] Sherby OD, Wadsworth J. In: Krauss G (Eds.). Deformation, processing and structure. Metals Park, Ohio: ASM; 1984, p. 355.

[24] Du N, Bower AF, Krajewski PE. Mater Sci Eng A 2010;18-19:4837-4846.

[25] Kulas MA, Green WP, Taleff EM, Krajewski PE, McNelly TR. Metall Mater Trans A 2005;36A:1249–1261.

[26] Chen IW. Scr Metall 1983 ;17:17-22.

[27] Toda H, Yamaguchi T, Nakawaza M, Aoki Y, Uesugi K, Suzuki Y, Kobayashi M. Mater Trans 2010;51:1288-1295.

[28] Talbot DEJ. Inter Metall Rev 1975;20:166–184.

[29] Cho HC, Yu J, Park IS. Metall Trans A 1992;23:201-210.

[30] Hanna MD, Greenwood GW. Acta Metall 1982;30 :719-724.

[31] Pilling J, Ridley N. Superplasticity in Crystalline Solids, London: The institute

of Metals; 1989.

Caption list

Fig. 1 3D views of particles and cavities in alloy HP. Note that only pores (red) and particles (green) were extracted and shown here.

Fig. 2 3D equivalent strain distributions at two different applied strain levels, ε_z, in alloy HP.

Fig. 3 Cavity volume fraction as a function of true strain. Each data was fitted to a line to calculate cavity growth rate, η.

Fig. 4 Relationships between local strain increment and the volume change of pores/cavities at an applied strain of 0.40 in alloy HP. Strain increment between applied strain of 0.28 ~ 0.40 is shown.

Fig. 5 Changes in mean diameter and volume fraction with applied strain, representing how cavities nucleated at various loading steps and pre-existing hydrogen micro pores grow in alloy HP.

Fig. 6 Cavity growth rate as a function of average cavity radius in alloy HP, showing the cavity growth parameters of cavities nucleated at various loading steps and pre-existing hydrogen micro pores.

Fig. 7 Histograms of pores/cavities measured at the final loading step in alloy HP. Cavities have been classified into pre-existing hydrogen pores and damage in (a). All the cavities have been separated depending on a loading step at which each cavity is nucleated in (b).

Fig. 8 3D perspective views of pores/cavities (both are shown in red) and particles (green) captured at the final loading step in alloy HP-C. A Grain boundary image (grey) has been superposed on (a) in (b).

Fig. 9 Histograms of cavities nucleated on grain boundaries and in grain interior in alloy

HP-C. These are further classified into heterogeneous and homogeneous nucleation in each figure.

Fig. 10 Consecutive 3D images of pores/cavities (both are shown in red) and particles (green) captured at the three different applied strain levels in ally HP-C. (d) is the final 3D image superposed on a grain boundary image (grey) captured at the same load.

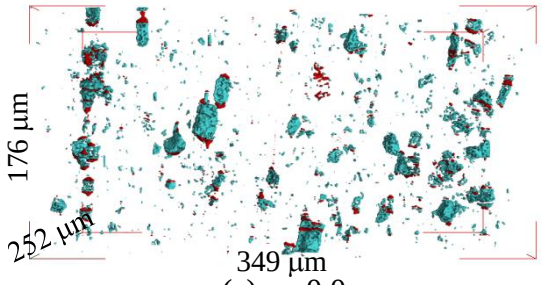

(a) ε_z=0.0

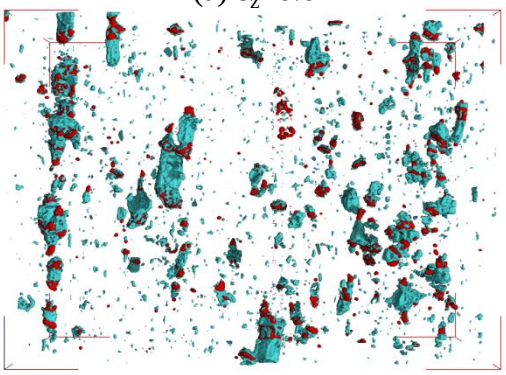

(b) ε_z=0.28

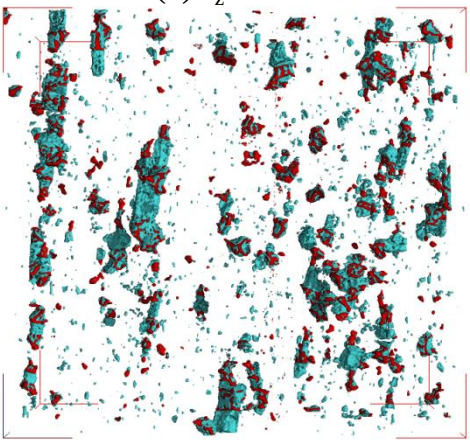

(c) ε_z=0.51

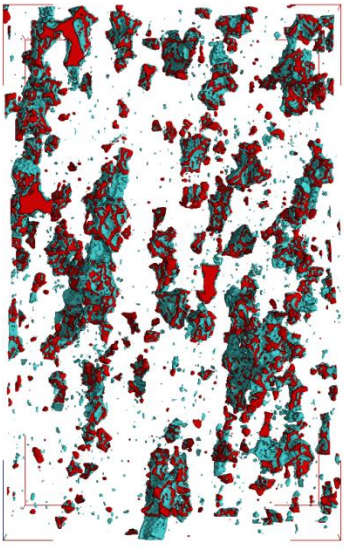

(d) ε_z=0.85

Fig. 1 3D views of particles and cavities in alloy HP. Note that only pores (red) and particles (green) were extracted and shown here.

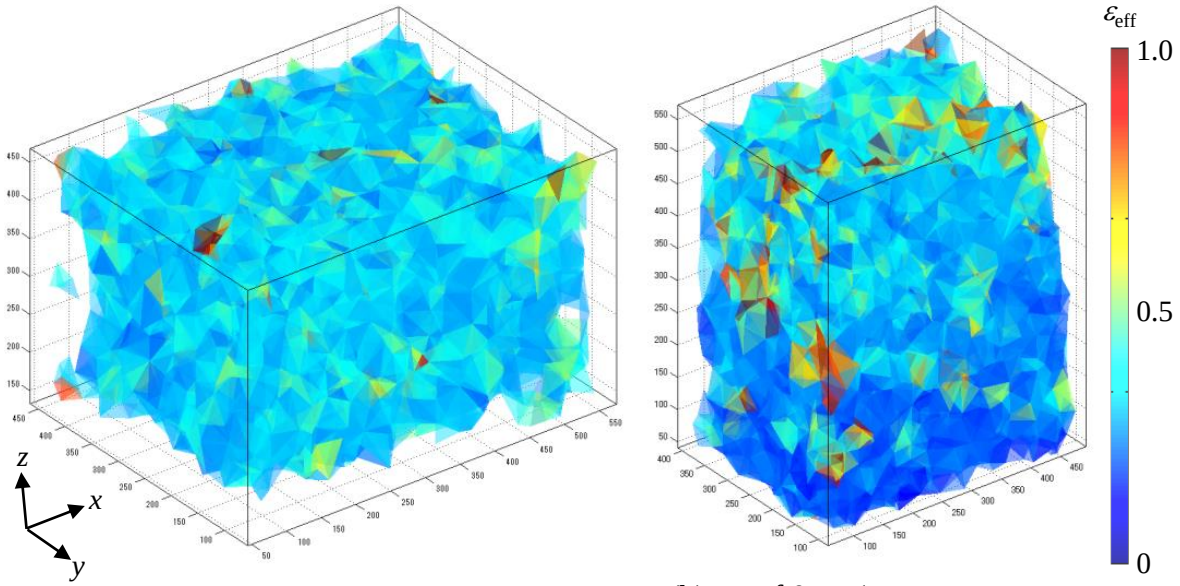

(a) ε_z of 0.28 (strain increment between ε_z = 0 ~ 0.28).

(b) ε_z of 0.74 (strain increment between ε_z = 0.51 ~ 0.74).

Fig. 2 3D equivalent strain distributions at two different applied strain levels, ε_z, in alloy HP.

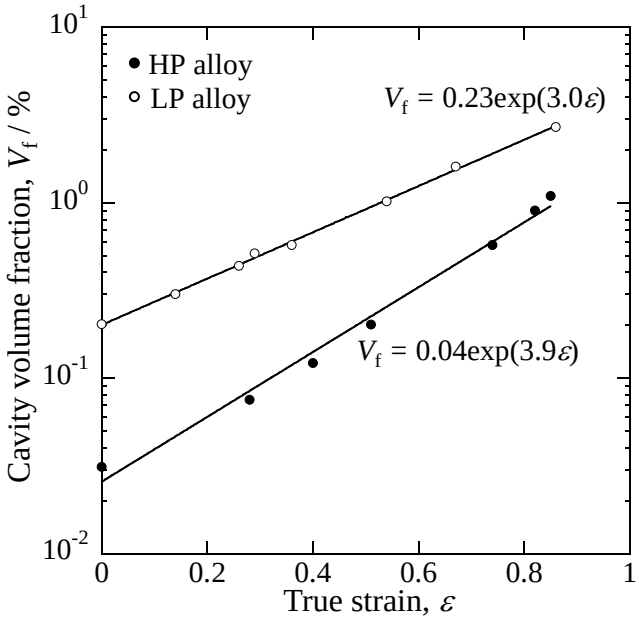

Fig. 3 Cavity volume fraction as a function of true strain. Each data was fitted to a line to calculate cavity growth rate, η.

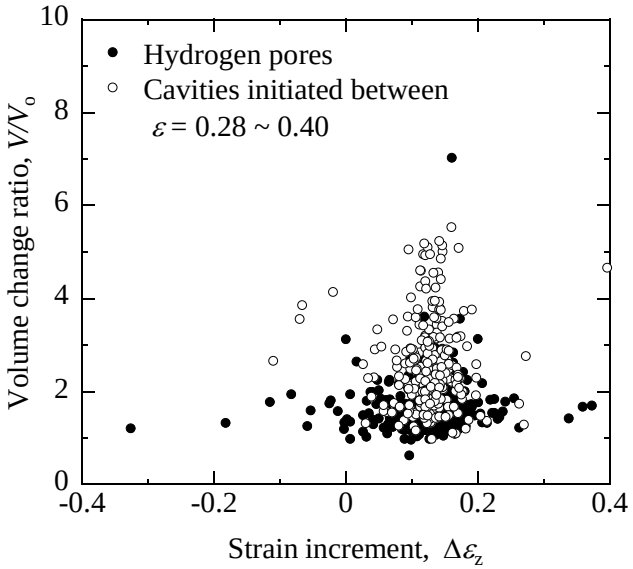

Fig. 4 Relationships between local strain increment and the volume change of pores/cavities at an applied strain of 0.40 in alloy HP. Strain increment between applied strain of 0.28 ~ 0.40 is shown.

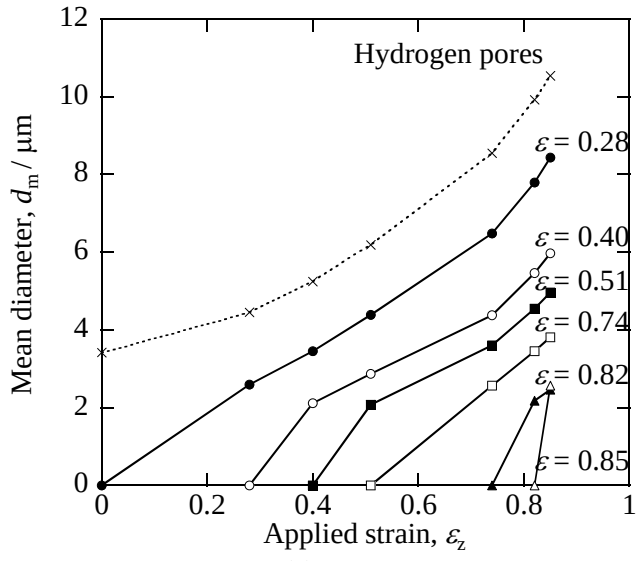

(a) Diameter

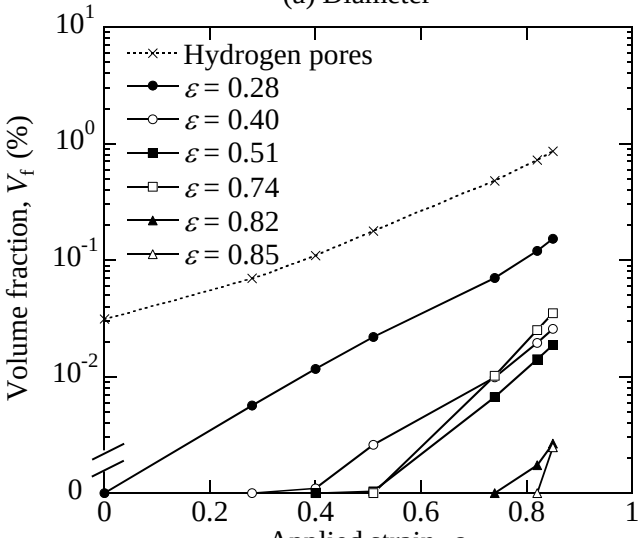

(b) Volume fraction

Fig. 5 Changes in mean diameter and volume fraction with applied strain, representing how cavities nucleated at various loading steps and pre-existing hydrogen micro pores grow in alloy HP.

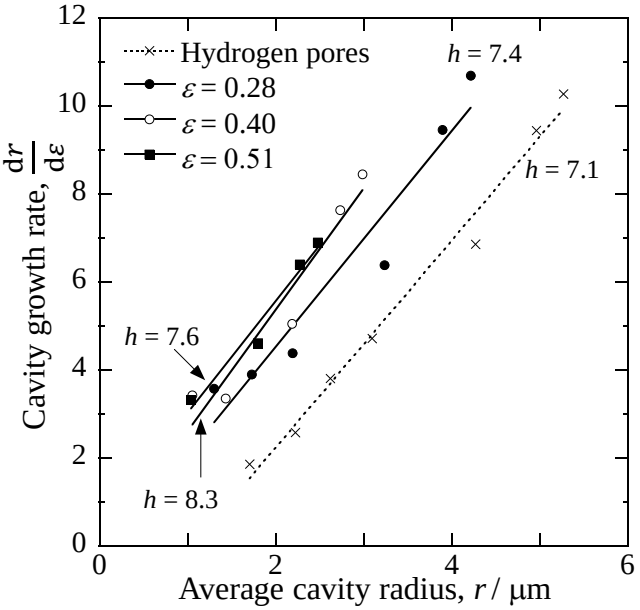

Fig. 6 Cavity growth rate as a function of average cavity radius in alloy HP, showing the cavity growth parameters of cavities nucleated at various loading steps and pre-existing hydrogen micro pores.

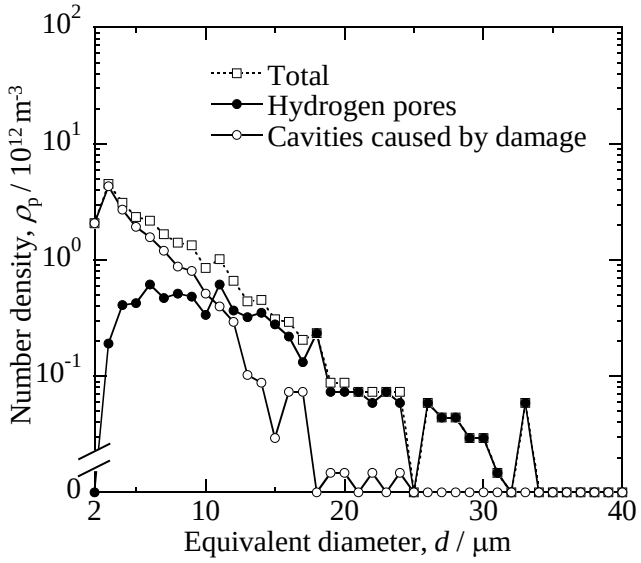

(a) Pores vs. cavities

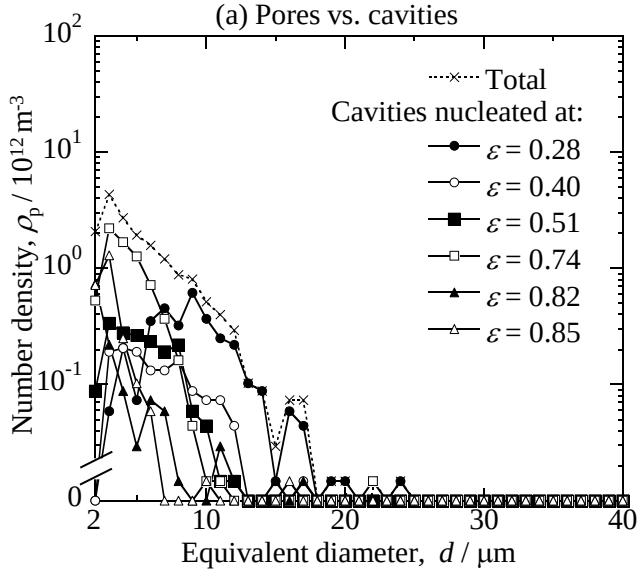

(b) Cavities nucleated at various loading steps

Fig. 7 Histograms of pores/cavities measured at the final loading step in alloy HP. Cavities have been classified into pre-existing hydrogen pores and damage in (a). All the cavities have been separated depending on a loading step at which each cavity is nucleated in (b).

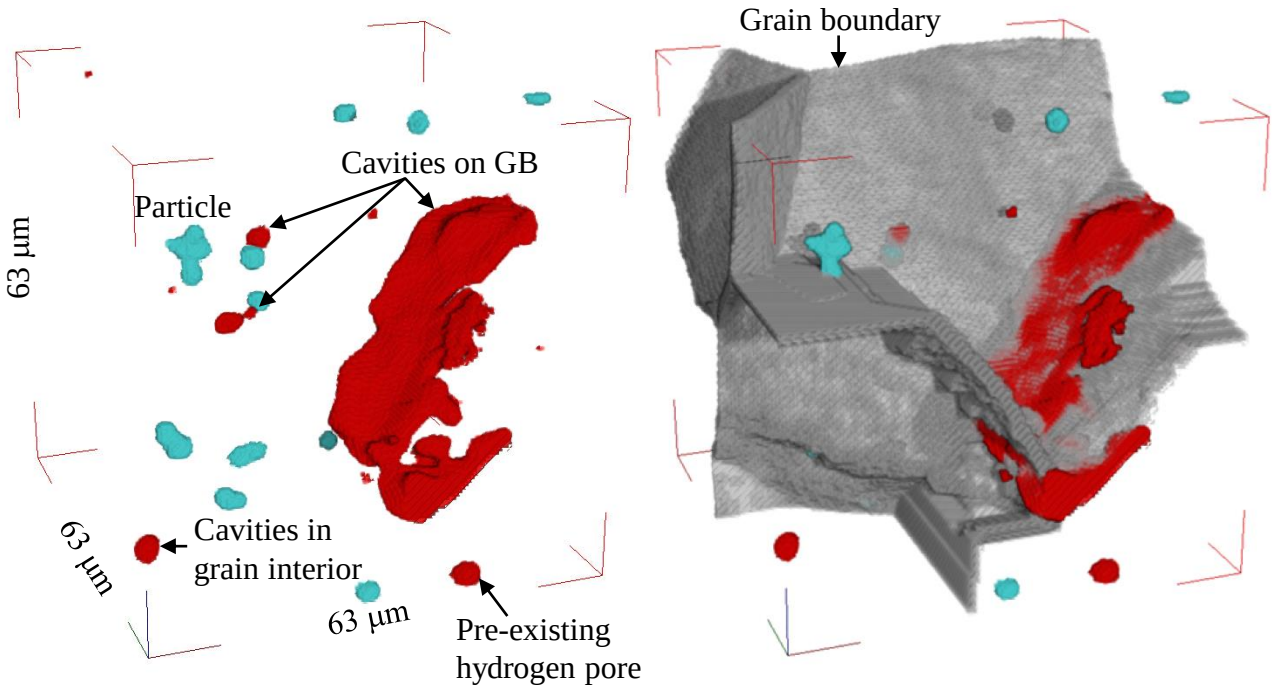

(a) Cavities and particles (b) Grain boundary image superposed on (a)

Fig. 8 3D perspective views of pores/cavities (both are shown in red) and particles (green) captured at the final loading step in alloy HP-C. A Grain boundary image (grey) has been superposed on (a) in (b).

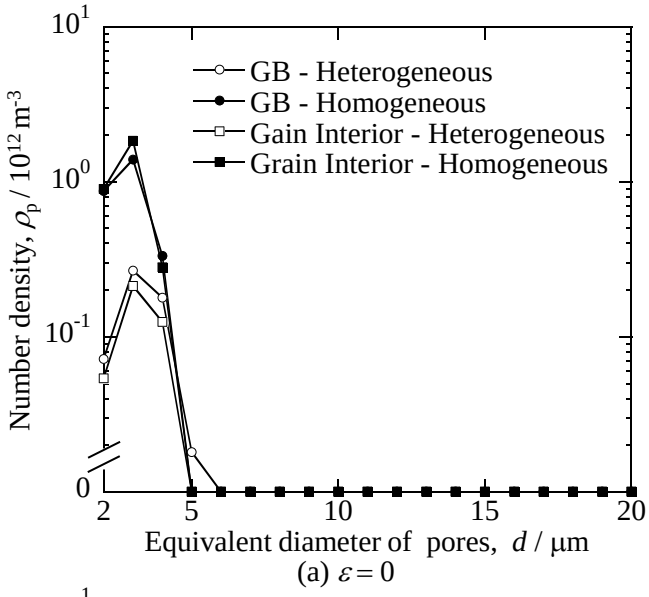

(a) $\varepsilon = 0$

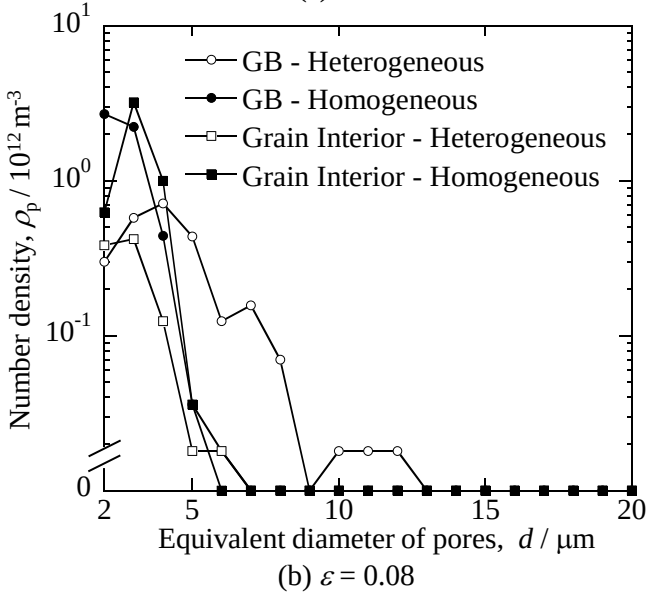

(b) $\varepsilon = 0.08$

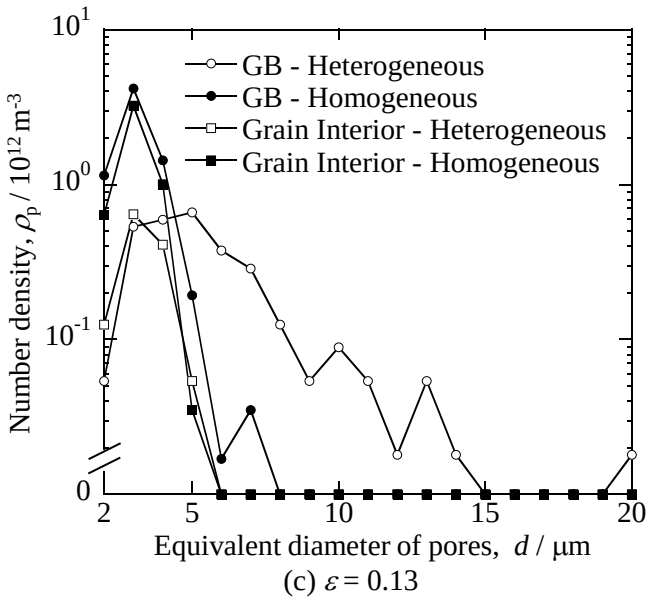

(c) $\varepsilon = 0.13$

Fig. 9 Histograms of cavities nucleated on grain boundaries and in grain interior in alloy HP-C. These are further classified into heterogeneous and homogeneous nucleation in each figure.

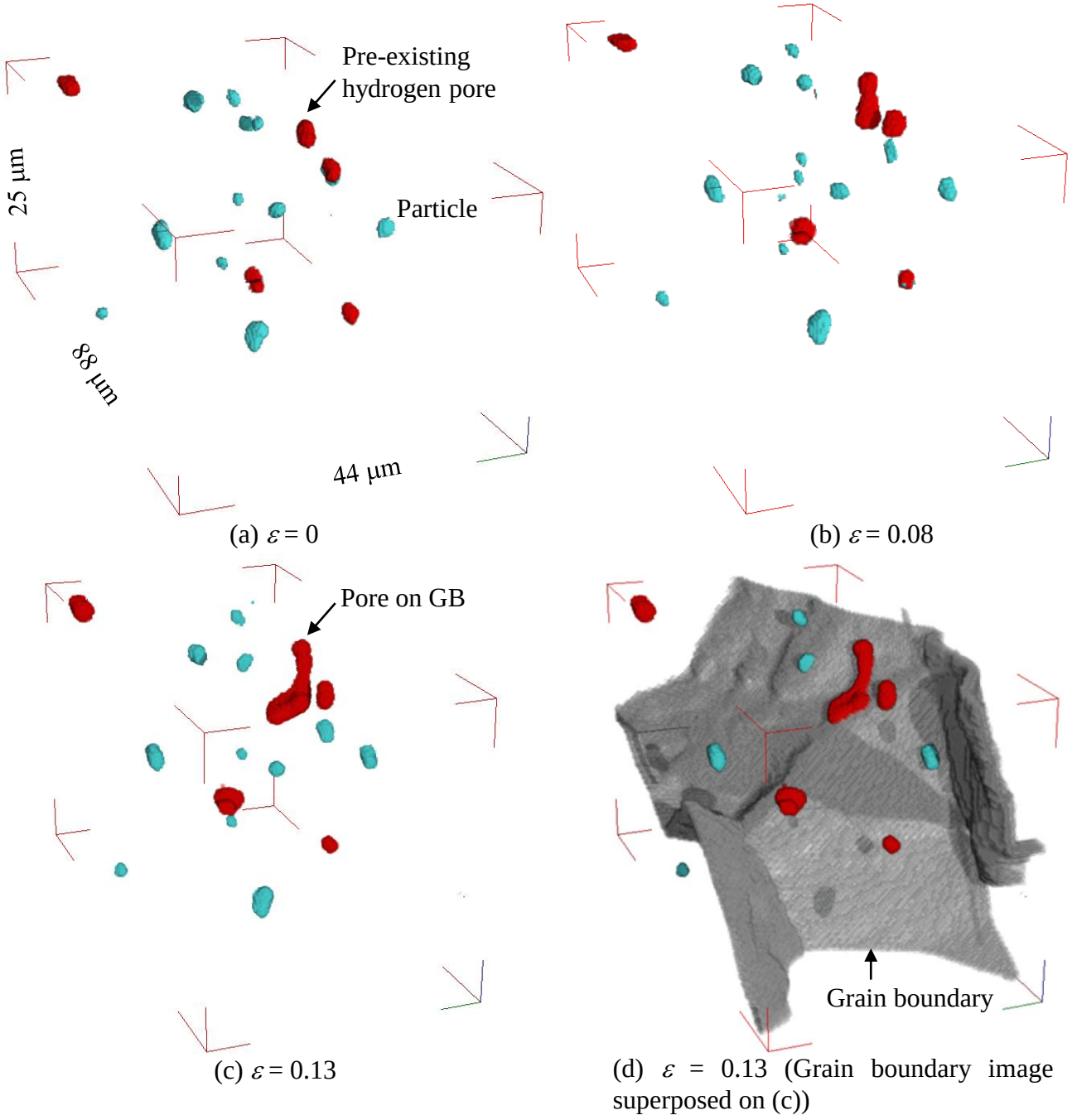

(a) $\varepsilon = 0$

(b) $\varepsilon = 0.08$

(c) $\varepsilon = 0.13$

(d) $\varepsilon = 0.13$ (Grain boundary image superposed on (c))

Fig. 10 Consecutive 3D images of pores/cavities (both are shown in red) and particles (green) captured at the three different applied strain levels in ally HP-C. (d) is the final 3D image superposed on a grain boundary image (grey) captured at the same load.